

# Quasiforbidden two-body Förster resonances in a cold Cs Rydberg gas

B. Pelle, R. Faoro,\* J. Billy,† E. Arimondo,\* P. Pillet, and P. Cheinet‡

*Laboratoire Aimé Cotton, UPR 3321 CNRS, Université Paris-Sud, ENS Cachan, Bâtiment 505, Campus d'Orsay, 91405 Orsay Cedex, France*

(Received 19 October 2015; published 12 February 2016)

Cold Rydberg atoms are known to display dipole-dipole interaction-allowed resonances, also called Förster resonances, which lead to an efficient energy transfer when the proper electric field is used. This electric field also enables resonances, which do not respect the dipole-dipole selection rules under zero field. A few of these quasiforbidden resonances have been observed but they are often overlooked. Here we show that in cold  $^{133}\text{Cs}$  atoms there is a large number of these resonances that display a significant transfer efficiency due to their strong interactions, even at low electric field. We also develop a graphical method enabling us to find all possible resonances simultaneously. The resulting dramatic increase in the total number of addressable resonant energy transfers at different electric fields could have implications in the search for few-body interactions or macromolecules built from Rydberg atoms.

DOI: [10.1103/PhysRevA.93.023417](https://doi.org/10.1103/PhysRevA.93.023417)

## I. INTRODUCTION

Resonant energy transfer in Rydberg atoms is well known to enhance two-body interactions between adjacent atoms [1], and is also called Förster resonance in analogy with the biological process known as fluorescence resonance energy transfer (FRET). These kinds of resonances have been studied to a great extent in Rydberg atoms originally in Refs. [1,2] and for different species in high electric fields [3,4]. They continue to be of interest [5–11] in the study of dipole blockade [12–16] and its induced entanglement [17,18], but also in studies on many-body [19] or more recently few-body [20,21] interactions, or even in an atom interferometer [22]. The dipole-dipole interactions between Rydberg atoms are also the basis of proposed approaches to realize quantum gates [23–26] or for the formation of novel long-range molecules [27–30].

While dipole-allowed Förster resonances have been studied in many different species, only a few quasiforbidden resonances have been observed in sodium and potassium [3,4]. These resonances exist in presence of an external static electric field leading to some coupling between Rydberg states in the transition dipole matrix, and where the eigenstates of the dipole-dipole Hamiltonian are no longer the pure eigenstates of the system. Then the dipole-dipole selection rules apply only partially, allowing the presence of several quasiforbidden two-body Förster resonances in addition to the dipole-allowed two-body Förster resonance(s). For instance, one specific resonance has been used in cesium to observe a four-body interaction [20]. These additional resonances could be of interest to increase the number of addressable resonances for possible quantum gates, for the creation of molecules from Rydberg atoms or for all applications based on few-body interactions. Moreover, these resonances, if not properly taken

into account, could modify the results of the previously described processes based on the dipole-allowed resonances. In addition, these resonances could introduce addressable resonances whenever no dipole-allowed resonance exists, for instance in cesium for  $n > 42$  or when starting from an initial  $ns$  state.

Within the present work, using cold  $^{133}\text{Cs}$  atoms excited to Rydberg states, we show the presence of a large number of quasiforbidden resonant energy transfers at low electric field, where we can identify each resonance and compute their dipole-dipole couplings. To determine their resonant Stark field, we apply a graphical method, which is well suited to predict resonances in the vicinity of the multiplicity and which is based on a combination of two Stark diagrams to solve the resonance condition.

## II. DIPOLE-DIPOLE INTERACTIONS

We consider two atoms A and B, separated by a distance  $R\mathbf{u}$ , with  $\mathbf{u}$  a unit vector, and originally both in a given Rydberg state  $|r_2\rangle$ . We also take into account two other Rydberg states  $|r_1\rangle$  and  $|r_3\rangle$ , almost equally separated from the initial state. We then define the two-atom state basis as  $|r_1r_3\rangle = 1/\sqrt{2}(|r_1\rangle_A|r_3\rangle_B + |r_3\rangle_A|r_1\rangle_B)$ , sketched in Fig. 1. The dipole-dipole interaction can couple the starting two-atom state  $|r_2r_2\rangle$  with other states, for instance  $|r_1r_3\rangle$ , and is then described by [31]:

$$\begin{aligned} \hat{V}_{\text{dd}} &= \langle r_2r_2 | \hat{H}_{\text{dd}} | r_1r_3 \rangle \\ &= \frac{1}{4\pi\epsilon_0} \frac{\hat{\boldsymbol{\mu}}_{r_1r_2} \cdot \hat{\boldsymbol{\mu}}_{r_2r_3} - 3(\hat{\boldsymbol{\mu}}_{r_1r_2} \cdot \mathbf{u})(\hat{\boldsymbol{\mu}}_{r_2r_3} \cdot \mathbf{u})}{R^3}, \end{aligned} \quad (1)$$

where  $\hat{V}_{\text{dd}}$  is the dipole-dipole interaction,  $\hat{H}_{\text{dd}}$  the associated Hamiltonian,  $\epsilon_0$  the electric vacuum permittivity,  $\hat{\boldsymbol{\mu}}_{r_1r_2} = \langle r_1 | \hat{\boldsymbol{\mu}} | r_2 \rangle$ , and  $\hat{\boldsymbol{\mu}}_{r_2r_3} = \langle r_2 | \hat{\boldsymbol{\mu}} | r_3 \rangle$  the transition dipole matrices between the involved atomic states with  $\hat{\boldsymbol{\mu}}$  the electric dipole moment operator. Due to selection rules on the angular part of the zero-field Rydberg wave functions and on parity conservation, the dipole moment operator introduces the selection rules  $\Delta l = \pm 1$  and  $\Delta m_j = 0, \pm 1$  in the zero-field

\* Alternate address: Dipartimento di Fisica, Università di Pisa, Largo Pontecorvo 3, I-56127 Pisa, Italy.

† Permanent address: Laboratoire Collisions Agrégats Réactivité, IRSAMC, Université de Toulouse-UPS and CNRS, UMR 5589, F-31062 Toulouse, France.

‡ patrick.cheinet@u-psud.fr

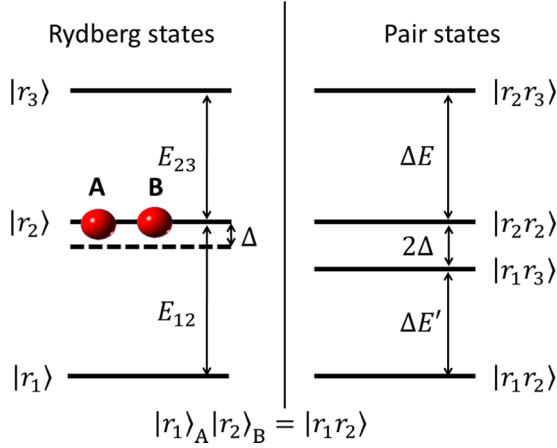


FIG. 1. Single-atom basis (left) and two-atom basis (right) for the description of interactions between atoms A and B having three Rydberg states  $|r_1\rangle$ ,  $|r_2\rangle$ , and  $|r_3\rangle$ .

Rydberg states basis, with  $l$  the orbital quantum number and  $m_j$  the second total angular momentum quantum number.

In general,  $|r_2 r_2\rangle$  and  $|r_1 r_3\rangle$  present an energy mismatch of  $2\Delta$  and the dipole-dipole interaction turns into an effective van der Waals interaction. The energy mismatch  $\Delta$ , also called Förster defect, is defined by  $\Delta = E_{12} - E_{23}$  with  $E_{ij}$  the energy difference between the involved Rydberg levels (see Fig. 1). In the rare degenerate case or when an electric field is used to Stark shift the levels into resonance, a strong dipole-dipole interaction is restored between the two atoms and a resonant energy transfer occurs from  $|r_2 r_2\rangle$  to  $|r_1 r_3\rangle$ . It can also be seen as a mutual exchange of excitation between the two atoms. The resonance condition is then expressed as follows, with  $E_i$  the energy of the state  $i$ :

$$(E_{r_3} - E_{r_2}) - (E_{r_2} - E_{r_1}) = 0 \Leftrightarrow \Delta = 0. \quad (2)$$

A well-known set of allowed two-body Stark-tuned Förster resonances in  $^{133}\text{Cs}$  is between  $np$  and  $ns$  states, as shown on the Fig. 2 and expressed as:

$$2 \times np \leftrightarrow ns + (n+1)s, \quad (3)$$

where  $n$  is the principal quantum number and  $s$ ,  $p$  denote the orbital quantum numbers. Those allowed resonances give for instance a dipole-dipole coupling of 112 MHz at  $1 \mu\text{m}$  for the

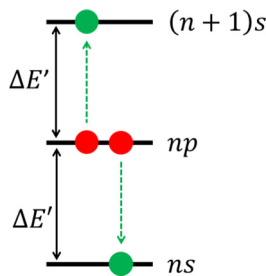


FIG. 2. Energy levels involved in the allowed two-body Förster resonance,  $2 \times np \leftrightarrow ns + (n+1)s$ , with its population transfer during the Förster resonance from the initial states (in red) to the final states (in green).

process of Eq. (3) with  $28p_{3/2}m_j = 3/2$  as the initial state, and 210 MHz at  $1 \mu\text{m}$  with  $32p_{3/2}m_j = 3/2$ .

In presence of a static electric field, the orbital quantum number  $l$  is no longer a good quantum number even if we will still use it as a convenient and unique way to label states. With a classical field  $\mathbf{F}$ , each pair of states  $|r_1\rangle$  and  $|r_2\rangle$  satisfying  $\Delta l = \pm 1$  is coupled due to the Stark effect [32]:

$$\langle r_1 | \hat{H}_F | r_2 \rangle = -\hat{\mu}_{r_1 r_2} \cdot \mathbf{F} \quad (4)$$

with  $\hat{H}_F$  the Stark Hamiltonian. The new eigenstates then contain a combination of  $l$  states instead of pure states. Then the selection rule on the orbital quantum number is relaxed and transitions for any  $\Delta l$  can be addressed with a strength depending on the  $l$ -mixing coupling. As an example to compare with the allowed Förster resonances, a quasiforbidden resonance such as

$$2 \times 28p_{3/2}m_j = 3/2 \leftrightarrow 28s_{1/2}m_j = 1/2 + 25f_{7/2}m_j = 1/2$$

reaches a dipole-dipole coupling of 6.65 MHz at  $1 \mu\text{m}$ .

The eigenstate energies  $E_i$  can be computed as a function of the applied electric field  $\mathbf{F}$  in a so-called Stark map, as shown in solid black in Fig. 3 in the upper vicinity of the  $28p_{3/2}m_j = 3/2$  state and where we only plot the absolute values  $|m_j|$ . The  $l \leq 5$  states in cesium are not degenerated with the other states because of the so-called quantum defect [31,32] originating from the interaction between the Rydberg electron and the ionic core. Then at low values of the electric field, those Rydberg states experience a quadratic Stark effect. On the contrary, states with higher  $l$  are degenerated in the multiplicity at low electric field and show a strong linear Stark effect. As we will use this Stark map to identify our quasiforbidden resonances, our numerical solution of the time-independent Schrödinger equation takes into account only the second total angular momentum quantum numbers  $|m_j| \leq 5/2$ . In the following, we will examine quasiforbidden resonances from initial states with  $m_j = 1/2$  or  $3/2$  while the selection rule  $\Delta m_j = 0, \pm 1$  is still preserved for dipole-dipole transitions.

In Fig. 3, we plot a graphical solution of the resonance condition occurring in a Förster resonance [see Eqs. (2) and (3)]. We transform the resonance condition  $2 \times E_{r_2} = E_{r_1} + E_{r_3}$  in  $E_{r_1} = 2 \times E_{r_2} - E_{r_3}$  and for the initial state  $|r_2\rangle = |28p_{3/2}m_j = 3/2\rangle$  we plot in dashed red the energy corresponding to  $2 \times E_{r_2} - E_{r_3}$ . The resonance condition is then fulfilled at any energy crossing of solid black and dashed red states. The resulting plot will be denoted as a resonance map. The advantage of this graphical solution compared to the usual pair state energy plots [33] lies in the simplicity to locate the quasiforbidden resonances in the vicinity of the multiplicity. Indeed when the energies of  $N$  states are calculated, for a pair state energy plot *a priori*  $N^2$  curves are necessary to verify all the possible resonances, while in our graphical method only  $2N$  curves are required. The basic idea of the usual pair state energy plot is that only a small number of resonances are present and only the authorized ones are plotted. We also acknowledge the work in Ref. [34] where a similar plot was used as we discovered during this paper redaction.

At moderate electric fields, the strongest quasiforbidden resonances appear when the initial state and one of the final one fulfill the  $\Delta l = \pm 1$  selection rule. Therefore we will focus

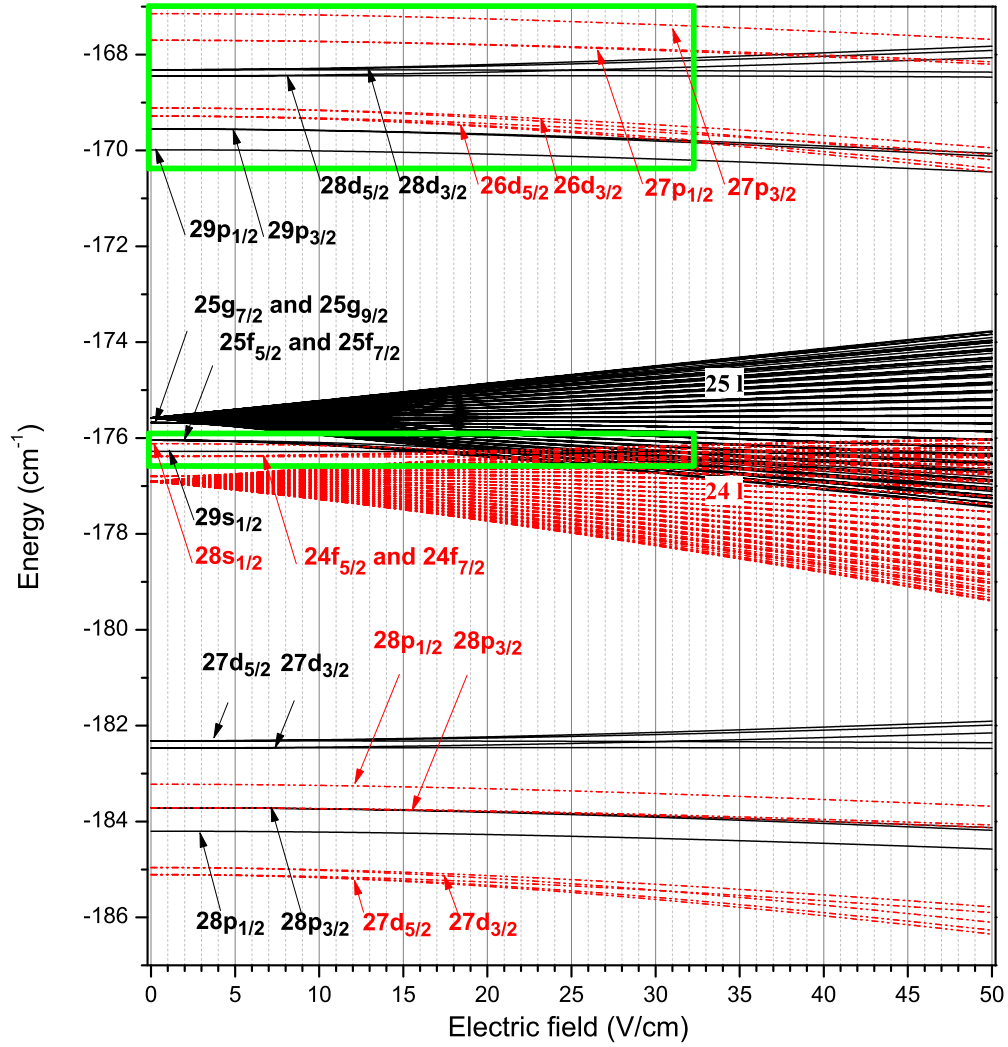


FIG. 3. Resonance map for the  $|r_2\rangle = |28p_{3/2}m_j = 3/2\rangle$  initial state. In solid black are plotted the eigenenergies  $E_{r_1}$  vs the applied external electric field  $F$ . In dashed red, we plot the energy corresponding to  $2 \times E_{r_2} - E_{r_3}$  to obtain a graphical solution of the resonance condition occurring in a Förster resonance. Only the absolute values of  $|m_j|$  are plotted. We emphasize the fact that the  $|r_2\rangle$  initial state curves in solid black and in dashed red are superimposed. In green, we explicit the areas represented in Figs. 4 and 5.

on resonances from the initial  $p$  state with at least one  $s$  or  $d$  final state as shown with light green triangles and blue circles on Fig. 4 and with purple diamonds on Fig. 5. Those symbols denote the multiple quasiforbidden Förster resonances, while a thick orange cross indicates an allowed Förster resonance.

To get the Stark field of the allowed Förster resonance starting from the  $28p_{3/2}m_j = 3/2$  initial state, we follow on Fig. 4 the dashed red curve labeled  $28s_{1/2}m_j = 1/2$  [corresponding to the energy of  $2 \times E(28p_{3/2}m_j = 3/2) - E(28s_{1/2}m_j = 1/2)$ ] until it crosses the solid black curve representing the  $29s_{1/2}m_j = 1/2$  state at  $F = 20.91$  V/cm. In the same way, we can identify the three main groups of quasiforbidden Förster resonances fulfilling the  $\Delta l = \pm 1$  condition for one of both final states. For the first group of resonances, we follow on Fig. 4 the dashed red curve labeled  $28s_{1/2}m_j = 1/2$  until it crosses the  $25f_{7/2}$  manifold in solid black at  $F = 11.04; 11.60; 14.00$  V/cm for the  $m_j = 1/2; 3/2; 5/2$  states, respectively. Here only states with a  $\Delta m_j = 0, \pm 1$  will be coupled in a dipole-dipole transition, eliminating the transition to the  $m_j = 7/2$

state. In the same group of resonances, the dashed red curve labeled  $28s_{1/2}m_j = 1/2$  crosses also the  $25f_{5/2}$  manifold in solid black at  $F = 11.64; 14.04; 20.38$  V/cm for the  $m_j = 1/2; 3/2; 5/2$  states respectively. If we continue along the dashed red curve labeled  $28s_{1/2}m_j = 1/2$ , we encounter quasiforbidden Förster resonances crossing the solid black  $25g_{9/2}$ ,  $25g_{7/2}$ ,  $25h_{11/2}$ , and  $25h_{9/2}$  manifolds around  $F \sim 20 - 21; 20 - 24; 25 - 27; 26 - 27$  V/cm respectively. For the second group of resonances, we follow on Fig. 4 the solid black curve labeled  $29s_{1/2}m_j = 1/2$  until it crosses the  $24f_{7/2}$  manifold in dashed red at  $F = 17.85; 19.03; 23.97$  V/cm for the  $m_j = 1/2; 3/2; 5/2$  states respectively, and the  $24f_{5/2}$  manifold in dashed red at  $F = 19.06; 24.01; 32.58$  V/cm for the  $m_j = 1/2; 3/2; 5/2$  states respectively. Then the solid black  $29s_{1/2}m_j = 1/2$  curve also crosses the dashed red  $24g_{9/2}$  and  $24g_{7/2}$  manifolds around  $F \sim 31; 31.5$  V/cm respectively. For the third group of resonances, we follow on Fig. 5 the dashed red curve labeled  $26d_{5/2}m_j = 1/2$  (the lowest state in the  $26d_{5/2}$  manifold) until it crosses the  $29p_{3/2}$  states in solid black at

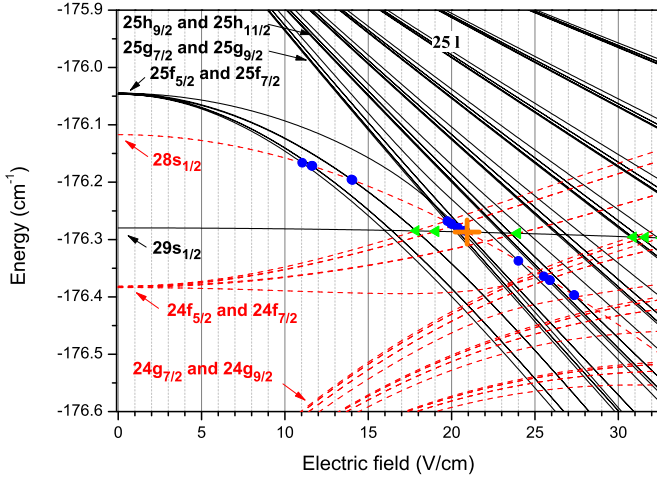


FIG. 4. Resonance map for the  $|r_2\rangle = |28p_{3/2}m_j = 3/2\rangle$  initial state in the vicinity of the  $29s$  and  $28s$  states. In solid black are plotted the eigenenergies  $E_{r_1}$  vs the applied external electric field  $F$ . In dashed red, we plot the energy corresponding to  $2 \times E_{r_2} - E_{r_3}$  to obtain a graphical solution of the resonance condition occurring in a Förster resonance. Here the thick orange cross indicates the allowed Förster resonance, the light green triangles and the blue circles show the multiple quasiforbidden Förster resonances transferring atoms to the  $29s$  and  $28s$  states respectively. Only the absolute values of  $|m_j|$  are plotted.

$F = 30.42; 31.99$  V/cm for  $m_j = 3/2; 1/2$  respectively. Similarly, the labeled  $26d_{5/2}m_j = 3/2$  dashed red curve crosses the  $29p_{3/2}m_j = 3/2$  state at  $F = 32.05$  V/cm.

To sum up, the first quasiforbidden Förster resonances of the groups detailed previously lead, for instance, to the population

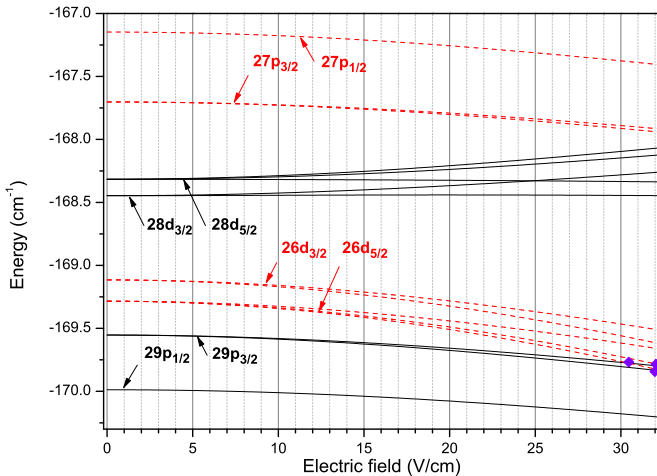


FIG. 5. Resonance map for the  $|r_2\rangle = |28p_{3/2}m_j = 3/2\rangle$  initial state in the vicinity of the  $28d$  and  $26d$  states. In solid black are plotted the eigenenergies  $E_{r_1}$  vs the applied external electric field  $F$ . In dashed red, we plot the energy corresponding to  $2 \times E_{r_2} - E_{r_3}$  to obtain a graphical solution of the resonance condition occurring in a Förster resonance. Here the purple diamonds show the few quasiforbidden Förster resonances transferring atoms to the  $29p$  and  $26d$  states. Only the absolute values of  $|m_j|$  are plotted.

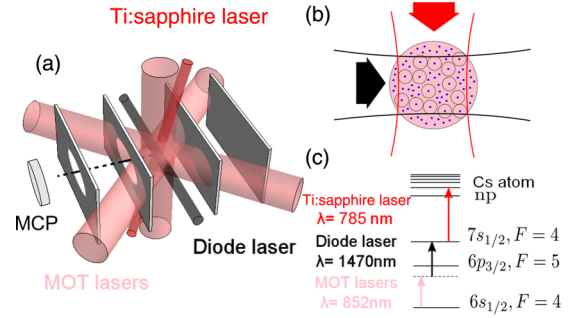


FIG. 6. (a) Experimental setup with a MOT in the center of four metallic wire mesh grids used to apply electric fields with voltages up to  $\pm 5$  kV. Rydberg atoms are excited at the cross section of the three-photon excitation lasers. The black dashed line defines the trajectory taken by the ionized Rydberg atoms toward the MCP detector. (b) Zoom on the excitation region at the laser cross section. (c)  $^{133}\text{Cs}$  energy levels used for the Rydberg excitation.

transfers:

$$2 \times 28p_{3/2}m_j = 3/2 \leftrightarrow 28s_{1/2}m_j = 1/2 + 25f_{7/2}m_j = 1/2$$

$$2 \times 28p_{3/2}m_j = 3/2 \leftrightarrow 29p_{3/2}m_j = 3/2 + 26d_{5/2}m_j = 1/2.$$

In those resonance equations, shown as an example, we see a transfer from a labeled  $p$  state to an  $f$  state (though transfers to higher orbital quantum number are possible) or with a transfer involving no change of the  $l$  state between the initial and final states. Those resonances correspond to quasiforbidden Förster resonances, which do not fulfill the  $\Delta l = \pm 1$  selection rule in presence of a low electric field.

We also calculate the strength of the dipole-dipole coupling for all the different quasiforbidden resonances found with the graphical resolution. The calculation is realized in the frozen gas regime (fixed atoms) [35], within the Born-Oppenheimer approximation, and considering a possible fixed angle  $\theta$  between the electric field axis and the interatomic axis. The total angular momentum of the system must be conserved but as the molecular rotational angular momentum can change, the sum of the  $m_j$  of the two atoms is not necessarily conserved [36].

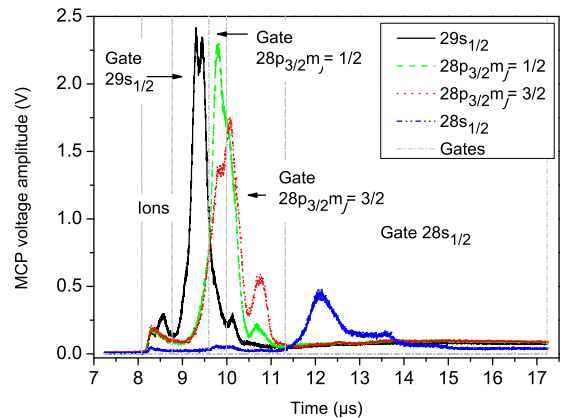


FIG. 7. Time-of-flight signal from selective field ionization (at  $V_{\text{ioniz}} = 2630$  V) to detect the  $np$ ,  $ns$  and  $(n+1)s$  signals on the MCP where each state has been directly excited at an electric field far from any Förster resonances.

TABLE I. Summary of dipole-dipole coupling strength for quasiforbidden resonances starting from the  $28p_{3/2}m_j = 1/2$  state.

Final states	$28s + 25f_{7/2}m'_j$		$28s + 25f_{5/2}m'_j$		$29s + 24f_{7/2}m'_j$		$29s + 24f_{5/2}m'_j$	
$m'_j$	1/2	3/2	1/2	3/2	1/2	3/2	1/2	3/2
Coupling at $1 \mu\text{m}$ (MHz)	12.25	8.95	10.4	7.7	15.5	9.98	12.45	7.05
Resonance (V/cm)	11.95	12.68	12.72	15.86	20.92	22.75	22.77	30.35
Final states	$28s + 25g_{9/2}m'_j$		$28s + 25g_{7/2}m'_j$		$29p_{3/2}m'_j + 26d_{5/2}m''_j$			
$m'_j$ or $(m'_j, m''_j)$	1/2	3/2	1/2	3/2	(3/2, 1/2)	(1/2, 1/2)	(3/2, 3/2)	
Coupling at $1 \mu\text{m}$ (MHz)	6.93	4.65	5.93	4.8	1.2	6.78	1.05	
Resonance (V/cm)	21.55	21.9	21.9	23.18	27.37	29.09	29.34	

 TABLE II. Summary of dipole-dipole coupling strength for quasiforbidden resonances starting from the  $28p_{3/2}m_j = 3/2$  state.

Final states	$28s + 25f_{7/2}m'_j$			$28s + 25f_{5/2}m'_j$			$28s + 25g_{9/2}m'_j$		
$m'_j$	1/2	3/2	5/2	1/2	3/2	5/2	1/2	3/2	5/2
Coupling at $1 \mu\text{m}$ (MHz)	6.65	10.3	14.05	0.81	0.7	0.55	5.15	5.15	7.35
Resonance (V/cm)	11.04	11.60	14.0	11.64	14.04	20.38	19.75	19.98	20.80
Final states	$28s + 25g_{7/2}m'_j$			$28s + 25h_{11/2}m'_j$			$28s + 25h_{9/2}m'_j$		$29p_{3/2}m'_j + 26d_{5/2}m''_j$
$m'_j$ or $(m'_j, m''_j)$	1/2	3/2	5/2	1/2	3/2	5/2	1/2	3/2	(3/2, 1/2)
Coupling at $1 \mu\text{m}$ (MHz)	0.11	0.29	0.7	3.05	6.45	8.95	0.17	0.33	2.6
Resonance (V/cm)	19.98	20.8	24.0	25.54	25.93	27.35	25.93	27.35	30.42
Final states	$29s + 24f_{7/2}m'_j$			$29s + 24f_{5/2}m'_j$			$29s + 24g_{9/2}m'_j$		$29s + 24g_{7/2}m'_j$
$m'_j$	1/2	3/2	5/2	1/2	3/2	5/2	1/2	3/2	1/2
Coupling at $1 \mu\text{m}$ (MHz)	9.0	12.45	15.05	0.64	0.59	0.26	3.9	7.25	0.17
Resonance (V/cm)	17.85	19.03	23.97	19.06	24.01	32.58	30.86	31.62	31.62

 TABLE III. Summary of dipole-dipole coupling strength for quasiforbidden resonances starting from the  $32p_{3/2}m_j = 1/2$  state.

Final states	$32s + 29f_{7/2}m'_j$		$32s + 29f_{5/2}m'_j$		$33p_{3/2}m'_j + 30d_{5/2}m''_j$			
$m'_j$ or $(m'_j, m''_j)$	1/2	3/2	1/2	3/2	(3/2, 1/2)	(1/2, 1/2)	(3/2, 3/2)	(1/2, 3/2)
Coupling at $1 \mu\text{m}$ (MHz)	27.1	18.05	22.45	13.35	0.98	6.0	0.9	4.83
Resonance (V/cm)	8.2	8.7	8.7	10.4	4.45	4.78	4.83	5.22

 TABLE IV. Summary of dipole-dipole coupling strength for quasiforbidden resonances starting from the  $32p_{3/2}m_j = 3/2$  state.

Final states	$32s + 29f_{7/2}m'_j$			$32s + 29f_{5/2}m'_j$		
$m'_j$	1/2	3/2	5/2	1/2	3/2	
Coupling at $1 \mu\text{m}$ (MHz)	29.0	22.5	26.8	0.8	1.03	
Resonance (V/cm)	7.5 (or 7.44) [37]	7.86	9.25	7.87	9.26	
Final states	$33p_{3/2}m'_j + 30d_{5/2}m''_j$					
$(m'_j, m''_j)$	(3/2, 1/2)	(1/2, 1/2)	(3/2, 3/2)	(1/2, 3/2)	(3/2, 5/2)	(1/2, 5/2)
Coupling at $1 \mu\text{m}$ (MHz)	1.73	0.05	4.18	0.08	7.55	0.16
Resonance (V/cm)	4.98	5.4	5.5	6.08	7.55	9.15

We can thus compute the dipole-dipole interaction for all the observed resonances. We then average the dipole-dipole coupling strength over this angle  $\theta$  and over the possible signs of all initial  $m_j$  while we sum the contribution of the possible signs of all final  $m_j$ , as they are degenerate in the electric field and the corresponding resonances will perfectly overlap. To compute this average, we assume a weak coupling regime for which the observed transfer is proportional to the square of the interaction strength. Tables I and II summarize the coupling for resonances starting from the  $28p_{3/2}m_j = 1/2$  state and  $28p_{3/2}m_j = 3/2$  state respectively. Tables III and IV display the same calculations for  $n = 32$ .

### III. EXPERIMENTAL SETUP

We realize a magneto-optical trap (MOT), which is located at the center of four parallel 60 mm by 130 mm wire mesh grids of 80  $\mu\text{m}$  thickness and 1 mm grid spacing [see Fig. 6(a)] [20]. In this MOT, cesium atoms are cooled down to 100  $\mu\text{K}$  and can be considered as frozen compared to the lifetime of the Rydberg state ( $\tau_{\text{rad}} \sim 60 \mu\text{s}$  for  $30p_{3/2}$  and  $\tau_{\text{rad}} \sim 21 \mu\text{s}$  for  $30s_{1/2}$  [38]). The inner pair of grids is spaced by  $1.88 \pm 0.02$  cm while the outer grids are 1.5 cm apart from the inner grids. At the beginning of the experiment sequence, a small electric field of several V/cm is applied on the inner grids.

We excite the atoms to Stark-shifted Rydberg states,  $nl$ , using a three-photon transition [see Fig. 6(c)]. We start from the MOT lasers and use two additional lasers to couple the states:  $6s \rightarrow 6p \rightarrow 7s \rightarrow nl$ . The  $6p \rightarrow 7s$  step uses 10 mW of a 1470 nm diode laser. A cw Ti:sapphire ring laser, providing roughly 600 mW on the atoms at 785 nm and locked on an ultrastable cavity, drives the  $7s \rightarrow nl$  transition. Those two lasers are focused to 300  $\mu\text{m}$  and 200  $\mu\text{m}$  spot diameters respectively and are perpendicularly overlapped in the atomic sample [see Fig. 6(b)]. Those beams are switched on for  $\tau_{\text{imp}} \sim 200$  ns, at a 10 Hz repetition rate, by two different acousto-optic modulators. We thus excite up to  $10^5$  atoms in the  $nl$  state within a 200  $\mu\text{m}$  diameter cloud having a typical density of  $10^{10} \text{ cm}^{-3}$ . We let the atoms interact *via* dipole-dipole interaction during a delay of  $\tau_{\text{delay}} \sim 1 \mu\text{s}$  after the Rydberg excitation and realize a selective field ionization (SFI) of the Rydberg atoms. We choose a short enough delay to avoid resonance broadening due to electric field inhomogeneities induced by ions created by Penning ionization and black-body radiations. A high-voltage ramp is then applied on the inner back grid, rising to  $V_{\text{ioniz}} = 2.6; 1.35$  kV for  $n = 28; 32$  in 4  $\mu\text{s}$  and ionizing the various Rydberg levels at different times. After a flight of 210 mm from the center of the trapped cloud, ions are detected by a microchannel plate (MCP) detector. The amplitude of the field ionization pulse is chosen to optimally isolate the  $np$  time-of-flight (TOF) signal from the other  $ns$  and  $(n+1)s$  signals [from Eq. (3)]. A typical TOF for all involved states in the allowed Förster resonance at  $n = 28$  is displayed on Fig. 7 where each state has been excited independently at an electric field far from any Förster resonance to avoid any transfer. We use these TOF references to define temporal gates corresponding to each state and compute the cross talks between the different gates. During a measurement, we only excite the atoms to the  $np_{3/2}$  states and extract the state population from their temporal gates to determine the

fraction of total population in different channels (corrected from their cross talks):  $ns$ ,  $np_{3/2}m_j = 1/2$ ,  $np_{3/2}m_j = 3/2$ , and  $(n+1)s$ . This analysis gives very accurate results on the population transfer for dipole-allowed Förster resonances [20]. For quasiforbidden resonances, other states are created and this analysis is no longer valid. An additional channel, the ion gate, was initially used to quantify the number of ions created before the field ionization, but it is used here to show atoms that are in an upper level than the  $(n+1)s$ . When atoms with higher-energy states are created, they add up in the ion gate. Their transfer is then generally underestimated. To get a more precise transfer efficiency, we would need to record a specific set of TOF references for each resonance. Nonetheless using our state population analysis, we can identify the resonances and estimate their relative amplitudes.

### IV. QUASIFORBIDDEN FÖRSTER RESONANCES

Tuning the static electric field, two-body Förster resonances can be scanned due to the Stark shift of Rydberg levels [3,4]. Those resonances are then detected by SFI since they produce changes in the population of the different states monitored on the TOF signals.

We plot in Fig. 8(a) the relative population of atoms transferred into various gates: the  $28s_{1/2}m_j = 1/2$  gate (in red), the  $29s_{1/2}m_j = 1/2$  gate (in blue), and in the ion gate (in black) depending on the applied electric field,  $F$ , from atoms initially prepared in the  $28p_{3/2}m_j = 1/2$  state. In order to determine the baselines, we take a reference measurement at an electric field where no resonance is expected, here at  $F = 19.8$  V/cm. On this graph, the allowed Förster resonance described below is expected and observed at  $F = 19.05$  V/cm:

$$2 \times 28p_{3/2}m_j = 1/2 \leftrightarrow 28s_{1/2}m_j = 1/2 + 29s_{1/2}m_j = 1/2.$$

Another expected resonance at  $F = 18.3$  V/cm is a three-body process described in Ref. [21]. All other resonances are quasiforbidden Förster resonances. Some of them concern a transfer to  $28s$  and another state with  $\Delta l > 1$ :

$$2 \times 28p_{3/2}m_j = 1/2 \leftrightarrow 28s_{1/2}m_j = 1/2 + 25f_jm'_j$$

$$2 \times 28p_{3/2}m_j = 1/2 \leftrightarrow 28s_{1/2}m_j = 1/2 + 25g_jm'_j.$$

Other ones correspond to a transfer to  $29s$  and  $24f$ :

$$2 \times 28p_{3/2}m_j = 1/2 \leftrightarrow 29s_{1/2}m_j = 1/2 + 24f_jm'_j.$$

For the resonances on Fig. 8,  $f_j$  takes the values  $f_{7/2}$  and  $f_{5/2}$ , while  $g_j$  is  $g_{9/2}$  or  $g_{7/2}$ , and  $m'_j$  is  $1/2$  or  $3/2$ .

In Fig. 9(a), we realize a similar measurement from atoms initially excited in the  $28p_{3/2}m_j = 3/2$  state, with a reference at  $F = 21.7$  V/cm. We find most of the formerly described resonances shifted in electric field. Indeed the  $28p_{3/2}m_j = 3/2$  state, higher in energy, requires a higher electric field to be Stark shifted down to the allowed resonance. On this graph, the following allowed Förster resonance is expected and observed at  $F = 20.91$  V/cm:

$$2 \times 28p_{3/2}m_j = 3/2 \leftrightarrow 28s_{1/2}m_j = 1/2 + 29s_{1/2}m_j = 1/2,$$

while the three-body process is expected at  $F = 22.05$  V/cm. Among the formerly described quasiforbidden Förster

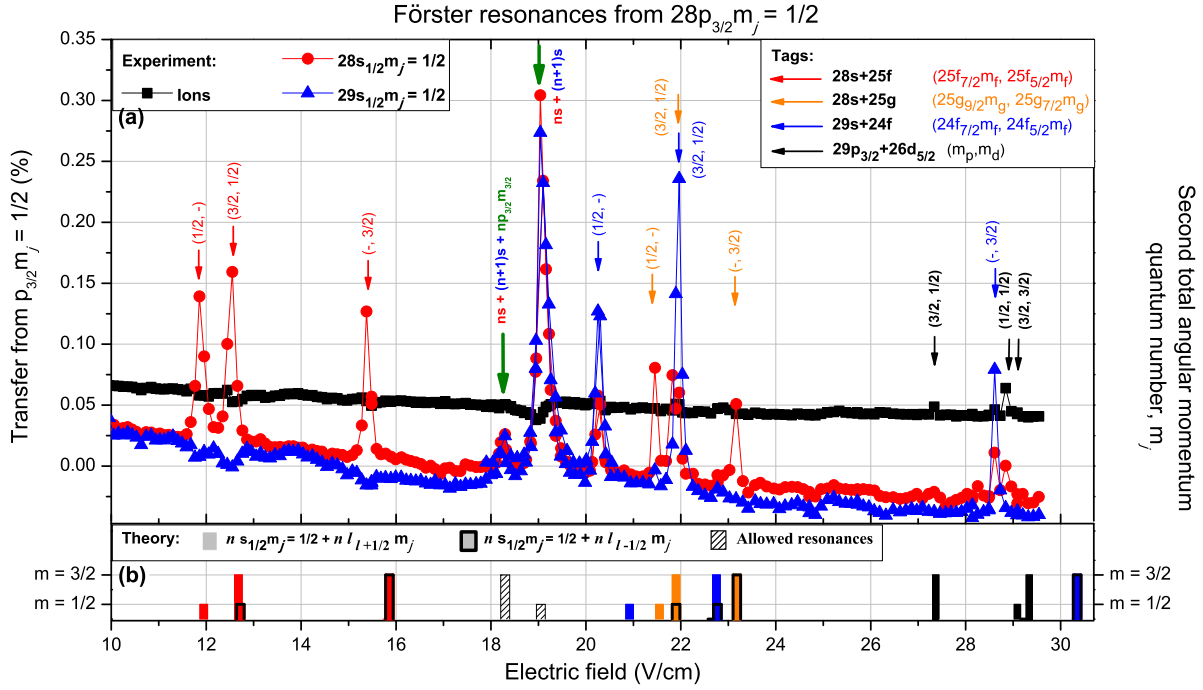


FIG. 8. Quasiforbidden Förster resonances around the allowed Förster resonance  $2 \times 28p_{3/2} m_j = 1/2 \leftrightarrow 28s_{1/2} m_j = 1/2 + 29s_{1/2} m_j = 1/2$  located at  $F = 19.05$  V/cm. (a) Experimental measurement where all final states of the different resonances are tagged. Ion gate is not included in the cross-talk correction so the mean baseline is not accurate. (b) Bar diagram representing the theoretical electric field resonance positions. We emphasize that the bar amplitude codes the projection  $m_j$  of the total angular momentum of the final state having  $J > 1/2$ . Moreover we distinguish the  $l_{+1/2}$  and  $l_{-1/2}$  final states adding a frame.

resonances, an additional group of resonances toward the labeled  $h$  states is also present

$$2 \times 28p_{3/2} m_j = 3/2 \leftrightarrow 28s_{1/2} m_j = 1/2 + 25h_j m'_j.$$

For the different resonances on Fig. 9,  $f_j$  takes the values  $f_{7/2}$  and  $f_{5/2}$ , while  $g_j$  is  $g_{9/2}$  or  $g_{7/2}$ ,  $h_j$  is  $h_{11/2}$  or  $h_{9/2}$ , and  $m'_j$  ranges from  $1/2$ – $5/2$ .

All theoretical predictions of those resonances are represented on Figs. 8(b) and 9(b) as bar diagrams. They define the locations in Stark field of Förster resonances thanks to the graphical method presented in Sec. II (see Figs. 4, 5 and Tables I–IV). Due to the large number of close resonances, we choose to code the projection of the total angular momentum quantum number  $m_j$  in the height of the bars (for the final states having a first total angular momentum quantum number  $J > 1/2$ ), i.e., in Fig. 8 the lower level represents  $m_j = 1/2$  and the higher level  $m_j = 3/2$ , while in Fig. 9 the lower level represents  $m_j = 1/2$ , the intermediate level  $m_j = 3/2$ , and the higher level  $m_j = 5/2$ .

From Figs. 8 and 9, we can see both allowed two-body Förster resonances, which are saturated close to 25% on each state  $ns$  and  $(n+1)s$ , giving a total transfer of 50%. This value is the expected saturation due to the random distribution in distances between Rydberg atoms, leading to a statistical average between pairs of atoms in  $np$  and pairs in  $ns$  and  $(n+1)s$ . The quasiforbidden Förster resonances appear clearly on this spectrum with a maximum change in the orbital quantum number from labeled  $p$  states to  $h$  states. They show for a single resonance an estimated non-negligible total transfer up to 30% with a large uncertainty

(see Sec. V), as only one of the two final states is correctly detected with a transfer of 15%. We also note that while this coupling is mainly due to dipole-dipole interactions allowed by the electric-field-induced  $l$  mixing, the resonances might contain additional dipole-multipole contributions [36], which cannot be distinguished experimentally here. We find those resonances close to the theoretical predictions, with a discrepancy compatible with the uncertainty in the quantum defects and in our field calibration (see Sec. V). In order to identify some of them, the analysis of the TOF signal shape was necessary to determine the resonance as discussed in Sec. V.

Moreover, quasiforbidden Förster resonances are expected in the vicinity of the allowed Förster resonance up to  $n = 32$ , as shown on Figs. 10 and 11 where references are taken at  $F = 5.6$  V/cm and  $F = 6.8$  V/cm. For higher  $n$ , the quasiforbidden resonances are expected further apart from the allowed resonance. At  $n = 32$ , the involved allowed Förster resonances are described by:

$$2 \times 32p_{3/2} m_j = 1/2 \leftrightarrow 32s_{1/2} m_j = 1/2 + 33s_{1/2} m_j = 1/2$$

$$2 \times 32p_{3/2} m_j = 3/2 \leftrightarrow 32s_{1/2} m_j = 1/2 + 33s_{1/2} m_j = 1/2.$$

They are expected and observed at  $F = 6.89$  V/cm and  $F = 7.55$  V/cm respectively, while forbidden resonances from labeled  $p$  states to  $f$  states show a resonant coupling up to roughly 8% in the  $32s$  gate. We also see quasiforbidden resonances similar to those seen on Fig. 5 which are described by the population transfer:

$$2 \times 32p_{3/2} m_j = 1/2 \leftrightarrow 33p_{3/2} m'_j + 30d_{5/2} m''_j$$

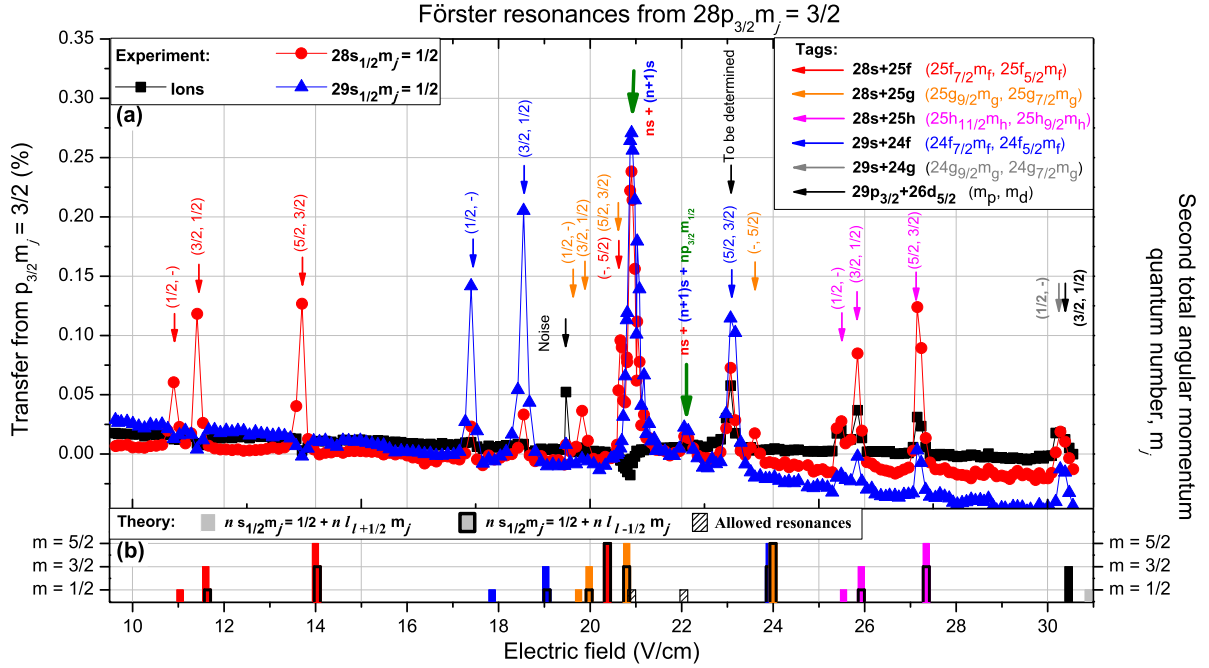


FIG. 9. Quasiforbidden Förster resonances around the allowed Förster resonance  $2 \times 28p_{3/2}m_j = 3/2 \leftrightarrow 28s_{1/2}m_j = 1/2 + 29s_{1/2}m_j = 1/2$  located at  $F = 20.91$  V/cm. (a) Experimental measurement where all final states of the different resonances are tagged. Ion gate is not included in the cross-talk correction so the mean baseline is not accurate. (b) Bar diagram representing the theoretical electric field resonance positions. We emphasize that the bar amplitude codes the projection  $m_j$  of the total angular momentum of the final state having  $J > 1/2$ . Moreover we distinguish the  $l_{l+1/2}$  and  $l_{l-1/2}$  final states adding a frame.

where  $m'_j$  and  $m''_j$  take the values  $1/2$  and  $3/2$  in Fig. 10, while in Fig. 11  $m''_j$  ranges from  $1/2$ – $5/2$ . Those resonances experiencing no change in their  $l$  state show also a maximum transfer efficiency of about 8% in the ion gate, corresponding to atoms transferred in the  $d$  state.

## V. DISCUSSION ON THE INTERPRETATION OF EACH RESONANCE

In order to identify the process involved in each resonance, we examine very carefully the TOF signal in order to identify each of the appearing Rydberg atom populations. In most

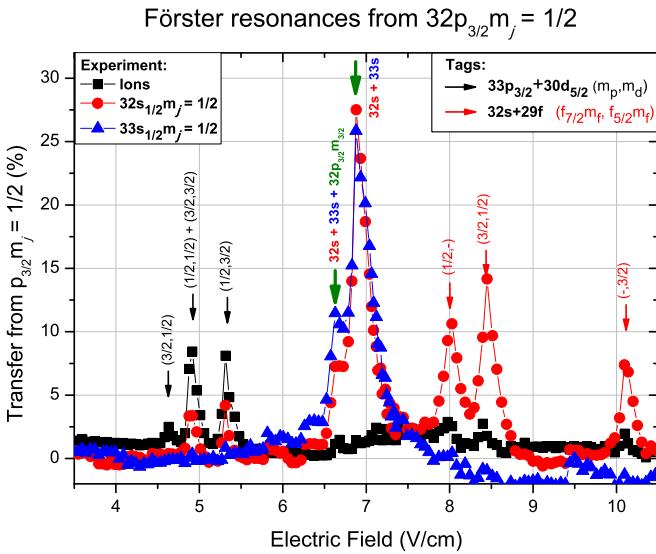


FIG. 10. Quasiforbidden Förster resonances around the allowed Förster resonance  $2 \times 32p_{3/2}m_j = 1/2 \leftrightarrow 32s_{1/2}m_j = 1/2 + 33s_{1/2}m_j = 1/2$  located at  $F = 6.89$  V/cm. Here is shown the experimental measurement where all final states of the different resonances are tagged. Ion gate is not included in the cross-talk correction so the mean baseline is not accurate.

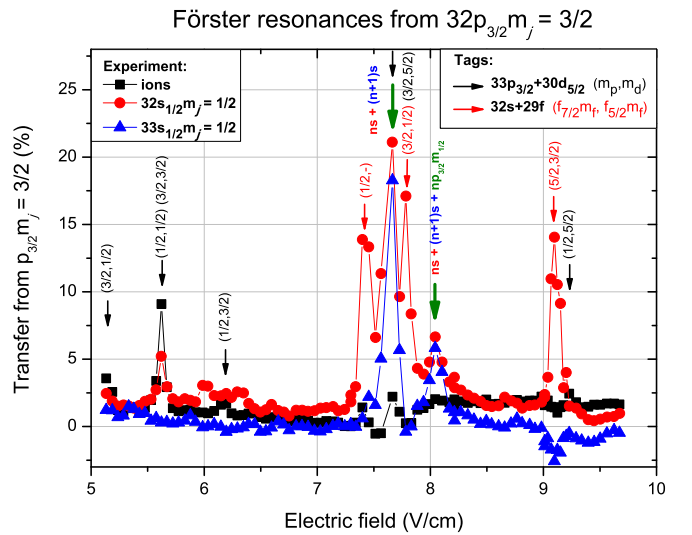


FIG. 11. Quasiforbidden Förster resonances around the allowed Förster resonance  $2 \times 32p_{3/2}m_j = 3/2 \leftrightarrow 32s_{1/2}m_j = 1/2 + 33s_{1/2}m_j = 1/2$  located at  $F = 7.55$  V/cm. Here is shown the experimental measurement where all final states of the different resonances are tagged. Ion gate is not included in the cross-talk correction so the mean baseline is not accurate.

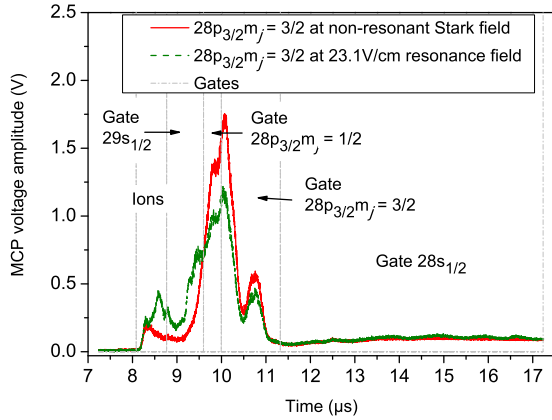


FIG. 12. TOF signal from SFI (at  $V_{\text{ioniz}} = 2630$  V) to detect the  $np$ ,  $ns$  and  $(n + 1)s$  signals where only the  $np$  states have been excited at a quasiforbidden resonant electric field  $F = 23.1$  V/cm (in green). We compare it to the reference signal (in red) shown on Fig. 7 and see some transfer into the ions, the  $(n + 1)s$  and  $ns$  gates. A lower state seems also to be present in the latter gate.

cases, this information combined with the expected patterns of the resonances enables their interpretation with no ambiguity, although the  $(n - 3)f$  states mainly overlap with the initial  $np$  state in the TOF signal. However, some situations are more complex when they involve none of the expected  $s$  state or when the resonances are very close. For instance, we will discuss the case of the quasiforbidden Förster resonance located at  $F = 23.1$  V/cm on Fig. 9 where the following energy exchange processes have been identified:

$$2 \times 28p_{3/2}m_j = 3/2 \leftrightarrow 29s_{1/2}m_j = 1/2 + 24f_{7/2}m_j = 5/2$$

$$2 \times 28p_{3/2}m_j = 3/2 \leftrightarrow 29s_{1/2}m_j = 1/2 + 24f_{5/2}m_j = 3/2.$$

Looking at the TOF signal on this resonance presented in Fig. 12, we can recognize the main  $28p$  state that has been excited (in both red and green traces). On the green trace taken at  $F = 23.1$  V/cm, we identify the presence of transferred atoms due to Förster resonance: in the  $29s$  gate we see the transferred  $29s$  atoms, whereas in the  $28s$  gate the atoms should correspond to the  $24f$  state [being the  $(n - 4)f$  state], which ionizes partially in this gate. In addition, we clearly observe a higher state in the ion gate, in comparison with the reference states on Fig. 7. As we do not know precisely the TOF of the  $24f$ , not observable with our excitation from the  $7s$  state, there might also be an even lower-energy state than the  $24f$  state in the  $28s$  gate in Fig. 12. It thus seems that a third process occurs at this field, which was not anticipated in Figs. 4 and 5. It could then involve states further in energy from the starting  $28p$  state, such as in the following resonance, which occurs at the same Stark field:

$$2 \times 28p_{3/2}m_j = 3/2 \leftrightarrow 27f_{7/2}m_j = 1/2 + 25d_{5/2}m_j = 3/2.$$

However, if we assume this resonance to be strong enough to be observed, we then expect to see other resonances involving all the different  $m_j$  but we do not observe them.

Another peculiar feature appearing on the Fig. 9 is the presence of some signal in the ion gate at  $F = 19.4$  V/cm although no resonance is expected. When trying to identify

the resonance in a TOF measurement, no transfer was observed. On other measurements not shown here, this signal is not present. Moreover, this signal corresponds to a single measurement point while resonances are generally broader. We thus interpret this data as an unexplained noisy measurement.

As we see on Figs. 8 and 9, there is a discrepancy between theory and measurements for some resonances. The two main uncertainties in this comparison between theory and experiment come from the quantum defect uncertainty used for the calculation and the uncertainty of the applied electric field in the experiment. The later is known at 1 or 2%, depending on the electric field, which corresponds to 0.6 V/cm at maximum in our measurements. Concerning the former, some resonances (to the final states  $s + f$  and  $s + g$ ) are systematically observed at a lower electric field than expected, which is coherent with the uncertainty of the quantum defects used in the calculation.

On Figs. 8–11, we observe a residual baseline drift probably due to slowly varying ionization path and residual black-body radiation transfer. One of the limitations of our state population analysis based on a cross-talk estimation lies in the fact that it is realized at one specific electric field (where there is no Förster resonance). Then when we change the electric field as plotted in Figs. 8–11, the cross talks might be a bit different. The first reason is that we are starting from a different initial voltage for the ionization ramp, which might lead to a different ionization path and then a different TOF shape for each of the state. We try to avoid this problem by setting the voltage to 0 V before the start of the ionization ramp but there might be a residual voltage. Then the second possible reason concerns the black-body radiation ionization, which might have a different efficiency depending of the applied electric field. Indeed by changing the applied electric field, we change the  $l$  mixing and allow then more transitions for the black-body radiations. This leads to a slightly different state population depending on the applied electric field, which translates to different cross talks as we change the applied electric field.

In the comparison between the observed transfer efficiencies of the quasiforbidden resonances and their calculated interaction strengths, most features are well reproduced. The small differences should be ascribed to few experimental and theoretical issues. First of all, because the gate analysis is not precisely adapted to each state produced by the various resonances, the measured transfers have an indetermination very hard to evaluate. Indeed for most of the resonances, we only detect correctly half of the final states (the  $s$  or the  $d$  states) with an uncertainty coming mainly from the imperfect cross-talk compensation between temporal gates. Then we assume that the quasiforbidden resonances transfer the same atom number in the second final states (the  $f, g, h$ , or the  $p$  states respectively), leading to a quite large total transfer efficiency uncertainty. A good example of this issue is shown in Fig. 7 where even a  $m_j$  state change modifies significantly the TOF output. This issue is particularly important for states as the  $(n - 3)f$  ones, which ionize mainly within the  $p$  gates. The second issue playing a role within the calculated strengths is the weak coupling assumption certainly not valid for the strongest resonances. In addition, the average over all signs of initial  $m_j$  with equal weights might not be valid as the experiment might generate an imbalance. Finally, we have not

considered the role of the small but finite MOT magnetic field, splitting the resonances by at most 10 mV/cm [11]. Within our setup, such a splitting cannot be observed directly and its role on the final transfer efficiency is not at all clear.

## VI. CONCLUSION

To conclude, we have seen that in the vicinity of the allowed two-body Förster resonance many quasiforbidden two-body Förster resonances are also present. They show an estimated total transfer up to 30% (taking into account both final states), with a calculated dipole-dipole coupling around 10% of the dipole allowed resonance coupling. In presence of a low electric field, the dipole-dipole coupling in those quasiforbidden Förster resonances allow population transfer with a change in the orbital quantum number from a labeled  $p$  state to a labeled  $h$  state or allow transfer involving no change of the  $l$  state between the initial and final states. We can assume that at a higher field  $\Delta l > 4$  resonances due to  $l$  mixing would appear as presented in Refs. [3,4]. We have also elaborated a graphical resolution of the resonance condition of Förster resonances, allowing to identify clearly the position of the different quasiforbidden Förster resonances. Then we calculated the dipole-dipole coupling strength for all of the observed quasiforbidden resonances, which correspond to their measured relative amplitudes.

When using the dipole-allowed Förster resonances for quantum computation, those quasiforbidden resonances could perturb the allowed resonance and should be taken into account to determine the total interaction strength in presence of an electric field. Moreover, those quasiforbidden two-body Förster resonances could be of interest in the case of potential processes requiring tunable interactions over a broad band of electric field, such as in the search for few-body interactions or to realize macromolecules built from Rydberg atoms. Indeed, they increase dramatically the number of addressable resonant energy transfers in the cesium atom with an efficiency about 10% of the well-known dipole-allowed resonances. For instance, it could increase the number of few-body transfer cascades as demonstrated in Ref. [20].

## ACKNOWLEDGMENTS

We acknowledge D. Comparat and A. Crubelier for useful discussions on dipole-dipole interactions. E.A. acknowledges the financial support by the Triangle de la Physique (Orsay). This work was supported by the Agence Nationale de la Recherche (ANR) under the program COCORYM (ANR-12-BS04-0013) and the EU Marie-Curie program ITN COHERENCE FP7-PEOPLE-2010-ITN-265031.

- 
- [1] K. A. Safinya, J. F. Delpéch, F. Gounand, W. Sandner, and T. F. Gallagher, Resonant Rydberg-Atom-Rydberg-Atom Collisions, *Phys. Rev. Lett.* **47**, 405 (1981).
  - [2] T. F. Gallagher, K. A. Safinya, F. Gounand, J. F. Delpéch, W. Sandner, and R. Kachru, Resonant Rydberg-atom-Rydberg-atom collisions, *Phys. Rev. A* **25**, 1905 (1982).
  - [3] R. Kachru, T. F. Gallagher, F. Gounand, P. L. Pillet, and N. H. Tran, Resonant collisions of Na  $nS$  and  $nD$  Rydberg atoms, *Phys. Rev. A* **28**, 2676 (1983).
  - [4] M. J. Renn, W. R. Anderson, and T. F. Gallagher, Resonant collisions of K Rydberg atoms, *Phys. Rev. A* **49**, 908 (1994).
  - [5] T. J. Carroll, K. Claringbould, A. Goodsell, M. J. Lim, and M. W. Noel, Angular Dependence of the Dipole-Dipole Interaction in a Nearly One-Dimensional Sample of Rydberg Atoms, *Phys. Rev. Lett.* **93**, 153001 (2004).
  - [6] C. S. E. van Ditzhuijzen, A. F. Koenderink, J. V. Hernández, F. Robicheaux, L. D. Noordam, and H. B. van Linden van den Heuvell, Spatially Resolved Observation of Dipole-Dipole Interaction between Rydberg Atoms, *Phys. Rev. Lett.* **100**, 243201 (2008).
  - [7] I. I. Ryabtsev, D. B. Tretyakov, I. I. Beterov, and V. M. Entin, Observation of the Stark-Tuned Förster Resonance between Two Rydberg Atoms, *Phys. Rev. Lett.* **104**, 073003 (2010).
  - [8] J. Nipper, J. B. Balewski, A. T. Krupp, B. Butscher, R. Löw, and T. Pfau, Highly Resolved Measurements of Stark-Tuned Förster Resonances between Rydberg Atoms, *Phys. Rev. Lett.* **108**, 113001 (2012).
  - [9] S. Ravets, H. Labuhn, D. Barredo, L. Béguin, T. Lahaye, and A. Browaeys, Coherent dipole-dipole coupling between two single atoms at a Förster resonance, *Nat. Phys.* **10**, 914 (2014).
  - [10] D. Barredo, H. Labuhn, S. Ravets, T. Lahaye, A. Browaeys, and C. S. Adams, Coherent Excitation Transfer in a Spin Chain of Three Rydberg Atoms, *Phys. Rev. Lett.* **114**, 113002 (2015).
  - [11] S. Ravets, H. Labuhn, D. Barredo, T. Lahaye, and A. Browaeys, Measurement of the angular dependence of the dipole-dipole interaction between two individual Rydberg atoms at a Förster resonance, *Phys. Rev. A* **92**, 020701(R) (2015).
  - [12] A. Gaëtan, Y. Miroshnychenko, T. Wilk, A. Chotia, M. Viteau, D. Comparat, P. Pillet, A. Browaeys, and P. Grangier, Observation of collective excitation of two individual atoms in the Rydberg blockade regime, *Nat. Phys.* **5**, 115 (2009).
  - [13] T. Vogt, M. Viteau, J. Zhao, A. Chotia, D. Comparat, and P. Pillet, Dipole Blockade at Förster Resonances in High Resolution Laser Excitation of Rydberg States of Cesium Atoms, *Phys. Rev. Lett.* **97**, 083003 (2006).
  - [14] D. Comparat and P. Pillet, Dipole blockade in a cold Rydberg atomic sample, *J. Opt. Soc. Am. B* **27**, A208 (2010).
  - [15] I. I. Ryabtsev, D. B. Tretyakov, I. I. Beterov, V. M. Entin, and E. A. Yakshina, Stark-tuned Förster resonance and dipole blockade for two to five cold Rydberg atoms: Monte Carlo simulations for various spatial configurations, *Phys. Rev. A* **82**, 053409 (2010).
  - [16] D. Barredo, S. Ravets, H. Labuhn, L. Béguin, A. Vernier, F. Nogrette, T. Lahaye, and A. Browaeys, Demonstration of a Strong Rydberg Blockade in Three-Atom Systems with Anisotropic Interactions, *Phys. Rev. Lett.* **112**, 183002 (2014).
  - [17] T. Wilk, A. Gaëtan, C. Evellin, J. Wolters, Y. Miroshnychenko, P. Grangier, and A. Browaeys, Entanglement of Two Individual Neutral Atoms Using Rydberg Blockade, *Phys. Rev. Lett.* **104**, 010502 (2010).

- [18] A. Gaëtan, C. Evellin, J. Wolters, P. Grangier, T. Wilk, and A. Browaeys, Analysis of the entanglement between two individual atoms using global Raman rotations, *New J. Phys.* **12**, 065040 (2010).
- [19] I. Mourachko, Wenhui Li, and T. F. Gallagher, Controlled many-body interactions in a frozen Rydberg gas, *Phys. Rev. A* **70**, 031401 (2004).
- [20] J. H. Gurian, P. Cheinet, P. Huillery, A. Fioretti, J. Zhao, P. L. Gould, D. Comparat, and P. Pillet, Observation of a Resonant Four-Body Interaction in Cold Cesium Rydberg Atoms, *Phys. Rev. Lett.* **108**, 023005 (2012).
- [21] R. Faoro, B. Pelle, A. Zuliani, P. Cheinet, E. Arimondo, and P. Pillet, Borromean three-body FRET in frozen Rydberg gases, *Nat. Commun.* **6**, 8173 (2015).
- [22] J. Nipper, J. B. Balewski, A. T. Krupp, S. Hofferberth, R. Löw, and T. Pfau, Atomic Pair-State Interferometer: Controlling and Measuring an Interaction-Induced Phase Shift in Rydberg-Atom Pairs, *Phys. Rev. X* **2**, 031011 (2012).
- [23] D. Jaksch, J. I. Cirac, P. Zoller, S. L. Rolston, R. Côté, and M. D. Lukin, Fast Quantum Gates for Neutral Atoms, *Phys. Rev. Lett.* **85**, 2208 (2000).
- [24] M. D. Lukin, M. Fleischhauer, R. Côté, L. M. Duan, D. Jaksch, J. I. Cirac, and P. Zoller, Dipole Blockade and Quantum Information Processing in Mesoscopic Atomic Ensembles, *Phys. Rev. Lett.* **87**, 037901 (2001).
- [25] L. Isenhower, E. Urban, X. L. Zhang, A. T. Gill, T. Henage, T. A. Johnson, T. G. Walker, and M. Saffman, Demonstration of a Neutral Atom Controlled-NOT Quantum Gate, *Phys. Rev. Lett.* **104**, 010503 (2010).
- [26] M. M. Müller, M. Murphy, S. Montangero, T. Calarco, P. Grangier, and A. Browaeys, Implementation of an experimentally feasible controlled-phase gate on two blockaded Rydberg atoms, *Phys. Rev. A* **89**, 032334 (2014).
- [27] C. H. Greene, A. S. Dickinson, and H. R. Sadeghpour, Creation of Polar and Nonpolar Ultra-Long-Range Rydberg Molecules, *Phys. Rev. Lett.* **85**, 2458 (2000).
- [28] V. Bendkowsky, B. Butscher, J. Nipper, J. P. Shaffer, R. Löw, and T. Pfau, Observation of ultralong-range Rydberg molecules, *Nature (London)* **458**, 1005 (2009).
- [29] W. Li, T. Pohl, J. M. Rost, S. T. Rittenhouse, H. R. Sadeghpour, J. Nipper, B. Butscher, J. B. Balewski, V. Bendkowsky, R. Löw, and T. Pfau, A homonuclear molecule with a permanent electric dipole moment, *Science* **334**, 1110 (2011).
- [30] M. Kiffner, H. Park, Wenhui Li, and T. F. Gallagher, Dipole-dipole-coupled double-Rydberg molecules, *Phys. Rev. A* **86**, 031401 (2012).
- [31] T. F. Gallagher, *Rydberg Atoms* (Cambridge University Press, Cambridge, 1994).
- [32] M. L. Zimmerman, M. G. Littman, M. M. Kash, and D. Kleppner, Stark structure of the Rydberg states of alkali-metal atoms, *Phys. Rev. A* **20**, 2251 (1979).
- [33] W. Li, P. J. Tanner, and T. F. Gallagher, Dipole-Dipole Excitation and Ionization in an Ultracold Gas of Rydberg Atoms, *Phys. Rev. Lett.* **94**, 173001 (2005).
- [34] C. S. E. van Ditzhuijzen, Dipole-dipole interaction between cold Rydberg atoms, Ph.D. thesis, University of Amsterdam, 2009 (unpublished).
- [35] I. Mourachko, D. Comparat, F. de Tomasi, A. Fioretti, P. Nosbaum, V. M. Akulin, and P. Pillet, Many-Body Effects in a Frozen Rydberg Gas, *Phys. Rev. Lett.* **80**, 253 (1998).
- [36] J. Deiglmayr, H. Saßmannshausen, P. Pillet, and F. Merkt, Observation of Dipole-Quadrupole Interaction in an Ultracold Gas of Rydberg Atoms, *Phys. Rev. Lett.* **113**, 193001 (2014).
- [37] At the theoretical resonance field, we observe a strong avoided crossing between the considered  $29f$  state and the  $33s$  state, which will then greatly enhance the calculated interaction. However, the observed separation between the quasiforbidden resonance and the allowed resonance demonstrates that this avoided crossing is further away. In order to compute the correct interaction, we had to modify the  $s$ -state quantum defect by  $10^{-4}$  to obtain the correct relative positions of the resonance (presented in brackets). For consistency with the other values in the table, we also display the original predicted resonance field.
- [38] I. I. Beterov, I. I. Ryabtsev, D. B. Tretyakov, and V. M. Entin, Quasiclassical calculations of blackbody-radiation-induced depopulation rates and effective lifetimes of Rydberg  $nS$ ,  $nP$ , and  $nD$  alkali-metal atoms with  $n \leq 80$ , *Phys. Rev. A* **79**, 052504 (2009).